Supporting Information

Electron transfer rate modulation with mid-IR in butadiyne-bridged donor-bridge-acceptor compounds

Kasun C. Mendis,[a] Xiao Li,[a] Jesús Valdiviezo,[b] Susannah D. Banziger,[e] Peng Zhang,[b] Tong Ren,[e] David N. Beratan,[b,c,d] and Igor V. Rubtsov[a*]

[a] *Department of Chemistry*, *Tulane University, New Orleans, LA 70118, USA*
[b] *Department of Chemistry*, *Duke University, Durham, North Carolina 27708, USA*
[c] *Department of Physics*, *Duke University, Durham, North Carolina 27708, USA*
[d] *Department of Biochemistry*, *Duke University, Durham, North Carolina 27710, USA*
[e] *Department of Chemistry*, *Purdue University, West Lafayette, Indiana 47907, USA*

Table of Content

S1. The matrix interpretation of the relationship between DAS and SAS

[*] To whom correspondence should be addressed. E-mail: irubtsov@tulane.edu

The equation 5 in the main text can be expressed in expanded matrix form as

$$\begin{pmatrix} P_{11} & \cdots & P_{j1} \\ \vdots & \ddots & \vdots \\ P_{1i} & \cdots & P_{ji} \end{pmatrix} \begin{pmatrix} SAS_1(\lambda) \\ \vdots \\ SAS_j(\lambda) \end{pmatrix} = \begin{pmatrix} DAS_1(\lambda) \\ \vdots \\ DAS_i(\lambda) \end{pmatrix} \qquad \text{(S1)}$$

The solution for these linear systems of equations can be expressed as in equation 6 and its matrix representation is

$$\begin{pmatrix} SAS_1(\lambda) \\ \vdots \\ SAS_j(\lambda) \end{pmatrix} = \begin{pmatrix} DAS_1(\lambda) \\ \vdots \\ DAS_i(\lambda) \end{pmatrix} \begin{pmatrix} P_{11} & \cdots & P_{j1} \\ \vdots & \ddots & \vdots \\ P_{1i} & \cdots & P_{ji} \end{pmatrix}^{-1} \qquad \text{(S2)}$$

We can evaluate the regular inverse of the preexponent matrix (P^{-1}) when the number of rates in lefthand side are equal to those of right hand side in Eq. 4 that results a square matrix of preexponents. When the number of rates in left hand side and right hand side are different, the preexponents matrix become non-square thus its inverse (P^{-1}) cannot be dierctly evaluated. In such cases Penrose Moore pseudoinverse (pinv) is used as the inverse of non-square matrices which can be shown as

$$SAS = DAS \times pinv(P) \ldots \qquad \text{(S3)}$$

Note that the number of SAS that can be recovered is limited by the quality of the experimental data.

S2. Evaluation of initial concentrations of the species in 2-pulse measurements

Relative concentrations of the species S2A, S2B, S1A and S1B prepared by the 400 nm pulse were computed using the UV-Vis absorption spectrum, giving S2 and S1 amounts, and DFT calculations to obtain the S1 and S2 amounts within each group of conformers, A and B. The UV-Vis absorption spectrum of D-C4-NAP shows two broad features around 400 nm, one peaking at ca. 460 nm, which is assigned mostly to the S1 absorption, and one peaking at 380 nm, which is assigned to the S2 absorption. The modeling of the absorption spectrum is shown in Fig. S1. The emission spectrum supports this assignment. Vibronic peaks were added in the modeling of the S1 and S2 absorption. Although they are only seen as minor shoulders in DCM, they are apparent in D-C4-NAP absorption spectra in other solvents, such as toluene and hexane. The computations do not predict well enough the oscillator strength of the UV peak at ca. 30,000 cm^{-1}.
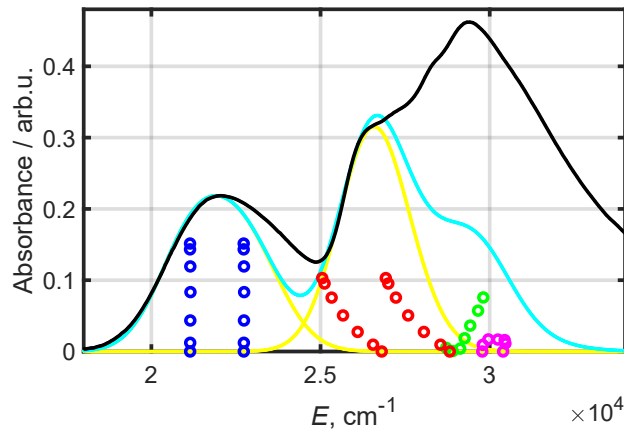
Figure S1. Absorption spectrum of D-C4-NAP in DCM (black line) and its modeling using DFT computed frequencies and oscillator strengths for S1 (blue circles), S2 (red circles), S3 (green circles), and S4 (cyan circles) absorption. Sets of circles of the same color show the frequencies and oscillator strength (Y-axis, arbitrary but comparable between the sets) computed for different torsion angles of (0, 15, 30, 45, 60, 75, and 90 degrees). The contributions of different torsion conformations were computed using the Boltzmann factor. Two sets of blue and red circles indicate the main and vibronic peaks for the S1 (blue) and S2 (red) absorption. The line spectra were broadened with Gaussian functions of slightly different widths for different sets (cyan line) to better match the experiment. The computed contributions from S1 and S2 absorption are shown by yellow lines. Note that the computed vibrational frequencies of the groups were scaled within 5% of their computed values to obtain a better match with the experiment.

Here the ratio of the amounts of S2 and S1 species, prepared by 400 nm excitation, was extracted from the modeling. For different modeling parameters, this ratio varied from 5 to 8 and was taken as 7 for the modeling of the TA experiments.

Closer look at oscillator strengths for $S_0 \rightarrow S_1$ and $S_0 \rightarrow S_1$ transitions (thicknesses of the lines in Fig. S2) local excited state (S_2) is bright at higher torsion angles while charge separated state (S_1) is bight at lower torsion angles. Thus, the observations for ET processes (or in the other words, dynamic formation of the CSS) are highly contributed from the conformers having higher torsion angles.
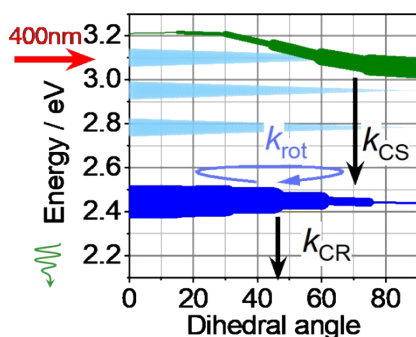

Figure S2. Electronic excited-state energy diagram for all torsion-angle conformers of D-C4-NAP in DCM. The thickness of the lines represents the oscillator strength for transitions of each conformer from ground state to corresponding excited state. The red arrow shows the energy values of UV excitation while black arrows indicate the charge separation (S_2 -> S_1 relaxation) and ground state recovery (S_1 -> GS relaxation) with corresponding labels for the rates (k_{CS} and k_{CS} respectively), and blue arrow indicates rotation with rate of k_{rot}. The lighter blue slices demonstrate the vibrational cooling occurs during S_2 -> S_1 relaxation.

S3. Analytical solutions of the 2-pulse experiments

The kinetic scheme for two pulse experiments (scheme 1) shows that both A and B group conformers undergo similar sequence of processes (charge separation and charge recombination) in same manner. Therefore, we can expect the analytical solutions for S2A and S1A has the same form as for analogous B species (S2B and S1B respectively) thus a more generalized kinetic scheme can be shown as in Fig. S3 where X can be A or B.

$$\text{S2X} \xrightarrow{k_X} \text{S1X} \xrightarrow{k_{CR}}$$

Figure S3. Generalized kinetic scheme required in 2-pulse measurements. Here X can be either A or B.

Since of the kinetic processes discussed throughout the text are first order in nature, the analytical solution for each species can be represented as a linear combination of exponentials (Eq. S4)

$$C(t) = \sum_m P_m \exp\left(-k_m t\right)$$

(S4)

where $C(t)$ is the time dependent concentration of a species and P_m terms are the preexponentials of each exponential term carrying k_m rate constant. P_m terms can be expressed as a multiplication of the contributions from initial concentrations (C_m^0) and factors ρ_m:

$$P_m = C_m^0 \rho_m$$

(S5)

There is only one ρ term appears in the solutions for the above kinetic scheme which is

$$\rho_X = \frac{k_X}{k_X - k_{CR}}$$

(S6)

Using the equations S4-S6, the complete analytical solutions for two pulse experiments can be written as

$$n_{S2X}(t) = n_{S2X}^0 \exp\left(-k_X t\right)$$

(S7)

$$n_{S1X}(t) = n_{S2X}^0 \rho_X \exp\left(-k_{CR} t\right) - n_{S2X}^0 \rho_X \exp\left(-k_X t\right) + n_{S1X}^0 \exp\left(-k_{CR} t\right)$$

(S8)

S4. Evaluation of initial concentrations of the species formed in the 3-pulse experiments

The 400 nm excitation produces S2A, S1A, S2B, and S2B species as discussed above, and they undergo above mentioned kinetic processes (scheme 1). After a specified t_1 delay, mid-IR beam interrogates. This mid-IR interrogation excites fractions of the species in excited electronic states by t_1 delay to corresponding excited C≡C stretching modes forming tr species. The initial concentrations of formed tr species ($C_{SnX}{}^{tr}(\theta)$, n can be 1 or 2) can be expressed in terms of the concentrations of the already prepared electronically excited species at t_1 delay (C_{SnX}), and the intensities for C≡C stretching modes ($\mu_{trnX}(\theta)^2$) as

$$C_{SnX}{}^{tr}(\theta) = \sum_{\theta \in Gr.X} C_{SnX} \cdot \mu_{trnX}(\theta)^2$$

(S9)

Here the concentrations of already prepared electronically excited species can be calculated using the analytical solutions for the two pulse experiments (Eq. S7 and S8).

4

S5. Analytical solution of the kinetic scheme to describe 3-pulse experiments

The analytical solution of the kinetic scheme shown in Scheme 3a and b of the main text is given in Eq. S10-S11.

$$n_{S1X^{tr}}(t) = n^0_{S1X^{tr}} exp(-k_1 t) \tag{S10}$$

$$n_{S1X^{h}}(t) = n^0_{S1X^{tr}} \rho_1 (exp(-k_3 t) - exp(-k_1 t)) \tag{S11}$$

Here $n_{S1X^{tr}}(t)$ and $n_{S1X^{h}}(t)$ stand for concentrations of species S1X^{tr} and S1X^{h}, where X can take values of A and B. The pre-factor, ρ, is given by

$$\rho_1 = \frac{k_1}{k_1 - k_3} \tag{S12}$$

The analytical solution of the kinetic scheme shown in Scheme 3c and d of the main text is given in Eq. S13-S16.

$$n_{S2X^{tr}}(t) = n^0_{S2X^{tr}} exp(-w_{1X} t) \tag{S13}$$

$$n_{S2X^{h}}(t) = n^0_{S2X^{tr}} \rho_{3X} (exp(-w_{2X} t) - exp(-w_{1X} t)) \tag{S14}$$

$$n_{S1X^{tr}}(t) = (n^0_{S1X^{tr}} + n^0_{S2X^{tr}}) exp(-k_1 t) - n_{S2X^{tr}}(t) \tag{S15}$$

$$n_{S1X^{h}}(t) = (n^0_{S1X^{tr}} + n^0_{S2X^{tr}}) \rho_1 (exp(-k_3 t) - exp(-k_1 t)) - n^h_{S2X}(t) \tag{S16}$$

where X can take values of A and B, $w_{1X} = k_1 + k^{tr}_X$, $w_{2X} = k_3 + k^h_X$, and the pre-factors are given by

$$\rho_2 = \frac{k_3}{k_1 - k_3} \tag{S17}$$

$$\rho_{3X} = \frac{k_1}{w_{1X} - w_{2X}} \tag{S18}$$

S6. Finding SAS of the species appearing in the 3-pulse experiments

S6.1. S1^{tr} and S1^{h} species and their relaxation rates

The SAS of S1A^{tr}, S1B^{tr}, S1A^{h}, and S1B^{h} were obtained from the DAS associated with the 3-pulse experiments at t_1 = 50 ps, denoted by $@50$ superscript. Application of Eq. 4 of the main text to these 3-pulse data results in the following equation:

$$n_{S1A^{tr}}^{@50}(t)SAS_{S1A^{tr}}(\lambda) + n_{S1B^{tr}}^{@50}(t)SAS_{S1B^{tr}}(\lambda) + n_{S1A^h}^{@50}(t)SAS_{S1A^h}(\lambda) + n_{S1B^h}^{@50}(t)SAS_{S1B^h}(\lambda)$$

$$= \sum_{i=1}^{2} DAS_i^{@50}(\lambda)\, exp(-k_i^{DAS@50}t)$$

(S19)

S6.2. S2B^{tr} and S2B^h species and modulated rates of slow ET (k_B^{tr} and k_B^h)

The 3-pulse data measured at $t_1 = 2.5$ ps are used to determine the modulated rates of slow ET, k_B^{tr} and k_B^h, and SAS of the S2B^{tr} and S2B^h species. Implementing Eq. 4 of the main text to these data results in Eq. S20, where $@2.5$ superscript denotes the DAS and concentrations measured at $t_1 = 2.5$ ps.

$$n_{S1A^{tr}}^{@2.5}(t)SAS_{S1A^{tr}}(\lambda) + n_{S1A^h}^{@2.5}(t)SAS_{S1A^h}(\lambda) + n_{S1B^{tr}}^{@2.5}(t)SAS_{S1B^{tr}}(\lambda) + n_{S1B^h}^{@2.5}(t)SAS_{S1B^h}(\lambda) + n_{S2B^{tr}}^{@2.5}$$
$$(t)SAS_{S2B^{tr}}(\lambda) + n_{S2B^h}^{@2.5}(t)SAS_{S2B^h}(\lambda)$$
$$= DAS_1^{@2.5}exp\left(-k_1^{DAS@2.5}t\right) + DAS_2^{@2.5}exp\left(-k_2^{DAS@2.5}t\right) + DAS_3^{@2.5}exp\left(-k_3^{DAS@2.5}t\right)$$

(S20)

The S1A species follows Scheme 3a of the main text; thus, the analytical solutions for the concentrations of resulting S1A^{tr} and S1A^h have the forms of Eq. S10 and Eq. S11, respectively. Because S2B and S1B species follow Scheme 3d and 3b of the main text, respectively, the analytical solutions for the concentrations of the resulting species S2B^{tr}, S2B^h, S1B^{tr}, S1B^h have the forms of the equations S13-S16. In Eq. S21 the left-hand side of Eq. S20 is rearranged, separating different exponential terms obtained by solving the kinetic scheme.

$$exp\left(-k_1 t\right)\sum_i P_i^{k_1}SAS_i + exp\left(-w_{1B}t\right)\sum_i P_i^{W_{1B}}SAS_i + exp\left(-k_3 t\right)\sum_i P_i^{k_3}SAS_i + exp\left(-w_{2B}t\right)\sum_i P_i^{W_{2B}}SAS_i$$
$$= DAS_1^{@2.5}exp\left(-k_1^{DAS@2.5}t\right) + DAS_2^{@2.5}exp\left(-k_2^{DAS@2.5}t\right) + DAS_3^{@2.5}exp\left(-k_3^{DAS@2.5}t\right)$$

(S21)

Here i designates S1A^{tr}, S1A^h, S2B^{tr}, S2B^h, S1B^{tr}, and S1B^h species, $w_{1B} = k_1 + k_B^{tr}$, $w_{2B} = k_3 + k_B^h$, and P terms are corresponding pre-exponents (see Eq. S10-S18). The mismatch in number of exponential terms in left-hand and right-hand sides of Eq S21 was using an approximation, $k_1 + k_B^{tr} = k_1^{DAS@2.5} \sim k_1$, discussed in main text, which leads to Eq. S22. Now the SAS of the S2B^{tr} and S2B^h species can be determined using the procedure outlined in Eq. 4-6 of the main text.

$$exp\left(-k_1^{DAS@2.5}t\right)\left(\sum_i P_i^{k_1}SAS_i + \sum_i P_i^{W_{1B}}SAS_i\right) + exp\left(-k_3 t\right)\sum_i P_i^{k_3}SAS_i + exp\left(-w_{2B}t\right)\sum_i P_i^{W_{2B}}SAS_i$$
$$= DAS_1^{@2.5}exp\left(-k_1^{DAS@2.5}t\right) + DAS_2^{@2.5}exp\left(-k_2^{DAS@2.5}t\right) + DAS_3^{@2.5}exp\left(-k_3^{DAS@2.5}t\right)$$

(S22)

S6.3. S2A^{tr} and S2A^h species and modulated rates of fast ET (k_A^{tr}, and k_A^h)

The 3-pulse data measured at t_1 = 0.5 ps are used to determine the modulated rates of fast ET, k_A^{tr} and k_A^h, and SAS of the S2A^{tr} and S2A^h species. Implementing Eq. 4 of the main text to these data results in Eq. S23, where $@0.5$ superscript denotes the DAS and concentrations measured at t_1 = 0.5 ps.

$$\sum_i n_i^{@0.5}(t)SAS_i(\lambda) = DAS_1^{@0.5}\exp\left(-k_1^{DAS@0.5}t\right) + DAS_2^{@0.5}\exp\left(-k_2^{DAS@0.5}t\right) + DAS_3^{@0.5}\exp\left(-k_3^{DAS@0.5}t\right)$$

(S23)

Here i designates S2A^{tr}, S2A^h, S1A^{tr}, S1A^h, S2B^{tr}, S2B^h, S1B^{tr}, and S1B^h species. Because ET in both groups (A and B) is taking place at this t_1 delay, the Schemes 3c-3d of the main text are used to describe the concentrations of tr and h species of S2A and S2B states (Eq. S13 and S14), while the S1 state concentrations are determined by equations Eq. S15 and S16.

To reduce the number of different exponential terms in the left-hand side of Eq. S23, the contributions of species with known dynamics and known SAS were transferred to the right-hand side of the equation and subtracted from the transient absorption data, as shown in Eqs. S24-S25.

$$\sum_j n_j^{@0.5}(t)SAS_j(\lambda) + \sum_k (\exp\left(-k_1t\right) * P_k^{k_1} + \exp\left(-k_3t\right) * P_k^{k_3})SAS_k$$
$$+ \sum_k (\exp\left(-w_{1A}t\right) * P_k^{w_{1A}} + \exp\left(-w_{2A}t\right) * P_k^{w_{2A}})SAS_k + \sum_l n_l^{@0.5}(t)SAS_l(\lambda) = TA(t)$$

(S24)

Here index j designates all B species, S2B^{tr}, S2B^h, S1B^{tr}, and S1B^h, index k designates S1A^{tr} and S1A^h, and index l designates S2A^{tr} and S2B^h.

$$TA(t) - \sum_j n_j^{@0.5}(t)SAS_j(\lambda) + \sum_k (\exp\left(-k_1t\right) * P_k^{k_1} + \exp\left(-k_3t\right) * P_k^{k_3})SAS_i = TA^r(t)$$

(S25)

The reduced TA spectra ($TA^r(t)$, Eq. S25) were globally fitted with an exponential decay function to determine w_{1A} and w_{2A} (see more details in Section S8). With determined w_{1A} and w_{2A}, Eq. S25 is rearranged to Eq. S26, which was solved using steps similar to those outlined for solving Eq. 4-6 of the main text. The solution results in determination of SAS of the S2A^{tr} and S2A^h species.

$$TA^r(t) - \sum_k (\exp\left(-w_{1A}t\right) * P_k^{w_{1A}} + \exp\left(-w_{2A}t\right) * P_k^{w_{2A}})SAS_i = \sum_l n_l^{@0.5}(t)SAS_l(\lambda) \qquad (S26)$$

S7. Reconstructed TA spectra using determined DAS and SAS

The validity of the approximations and consistency of the obtained SAS was checked by reconstructing TA spectra from the determined SAS. Such comparison was performed for the 2-pulse experiments, showing precise match, and for 3-pulse experiments for all t_1 and t_2 values accessed in the experiments. For the comparison, the TA spectra were constructed from DAS components (Eq. 1) as well as from SAS components (Eq. 2). Figure S4 shows such comparison for the 3-pulse measurement at t_1 = 50 ps. The two spectra for each delay are shown by the same color but with different symbols (circles for SAS and crosses for DAS). A precise match was found for the experiments at t_1 = 50 ps, as expected. A similar comparison of the reconstructed spectra is shown in Figure S5-S6 for the experiments at t_1 = 2.5

and 0.5 ps. A close match of the reconstructed spectra is observed (Fig. S5 and S6), indicating that the taken assumptions did not change the overall spectral features significantly.

Figure S6 shows two spectral reconstructions, one for the two-component fit of the 3-pulse measurement at $t_1 = 0.5$ ps (panel a) and one for a single-component fit (panel b). A similarly good match for the single-component fit, as for the two-component fit, confirms the validity of a single-component approximation.
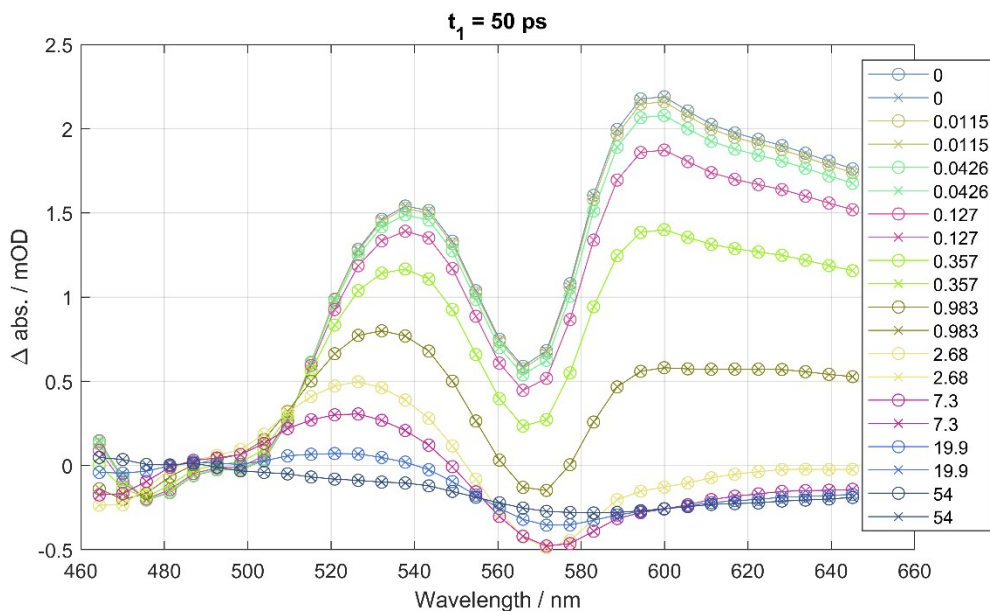

Figure S4. TA spectra for 3-pulse experiments at $t_1 = 50$ ps at specified t_2 delays in ps (see inset), reconstructed from SAS (connected circles) and DAS (connected crosses).
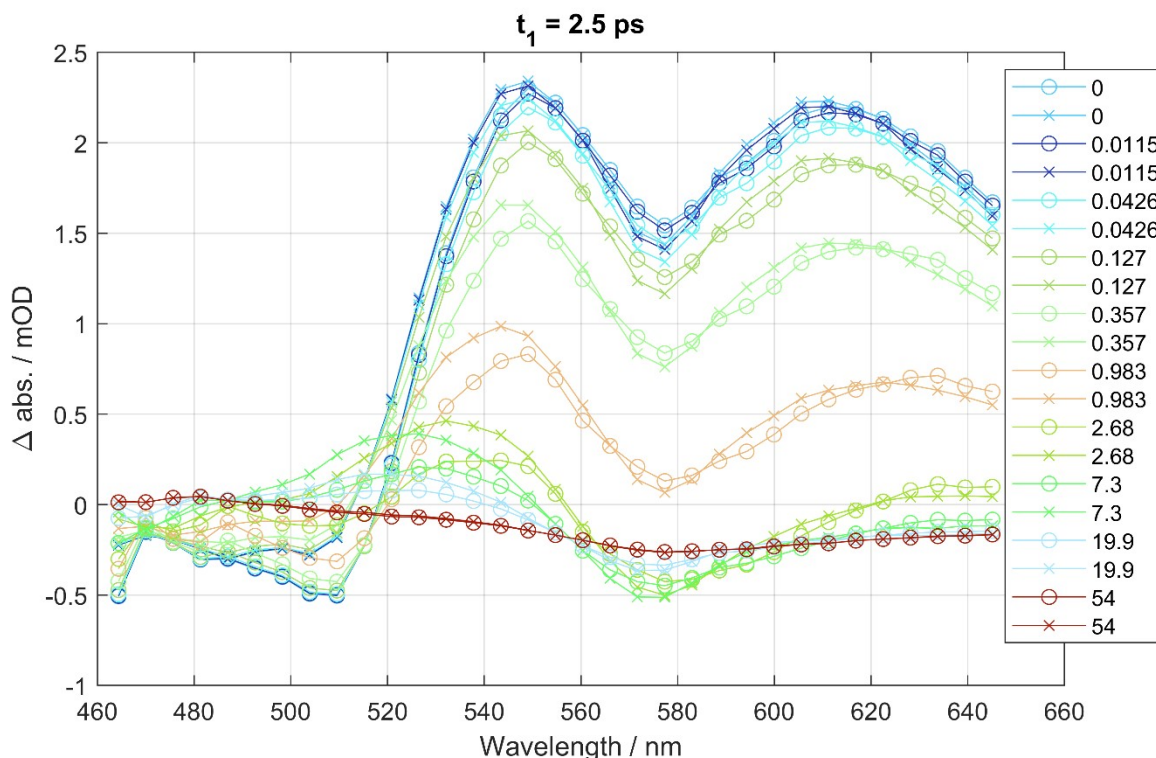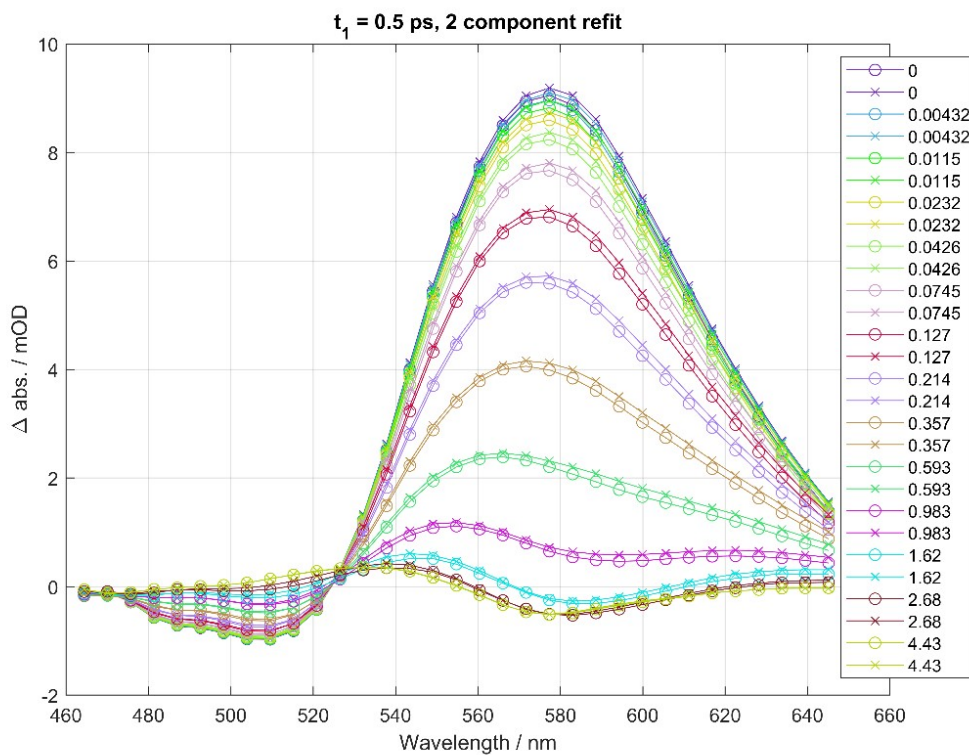
Figure S5. TA spectra for 3-pulse experiments at t_1 = 2.5 ps at specified t_2 delays in ps (see inset), reconstructed from SAS (connected circles) and DAS (connected crosses).
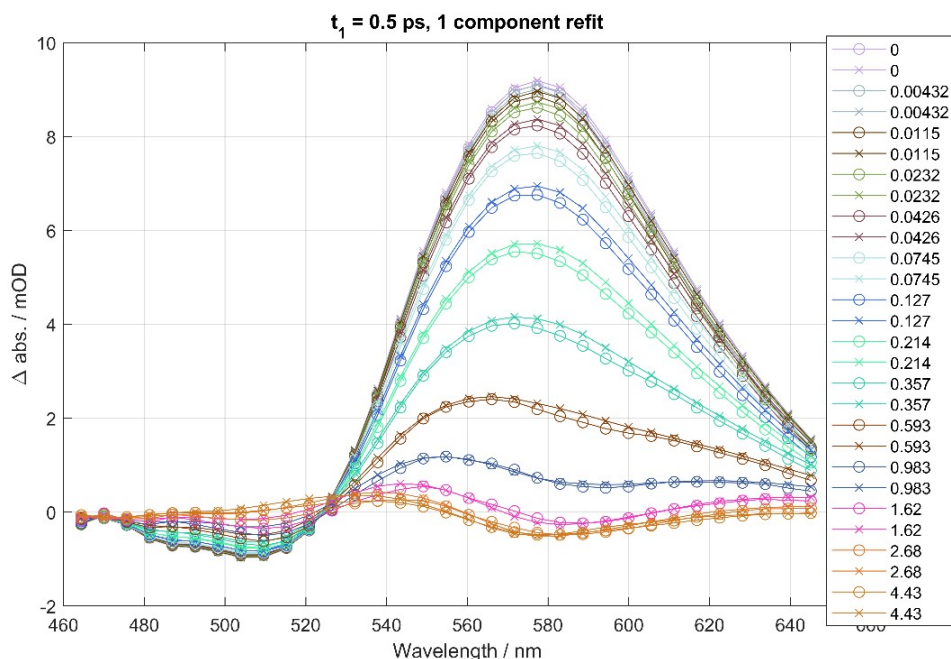
(a)

(b)

Figure S6. TA spectra for 3-pulse experiments at t_1= 2.5 ps at specified t_2 delays in ps (see inset), reconstructed from SAS (connected circles) and DAS (connected crosses) for (a) two-component, and (b) one-component fits.

S8. Reduced TA spectra and reconstructed DAS in the t_1=0.5 ps experiments

Reduced TA spectra are determined for t_1 = 0.5 ps to simplify the expression for Eq. 4 by taking into account the known contributions (Eq. S25), as described in Section 6.2. The spectral shape of the reduced TA spectra (Fig. S7) is similar to the shape of the fast DAS component for t_1 = 0.5 ps, reflecting the dominant contribution of the fast ET to the signals at t_1 = 0.5 ps.
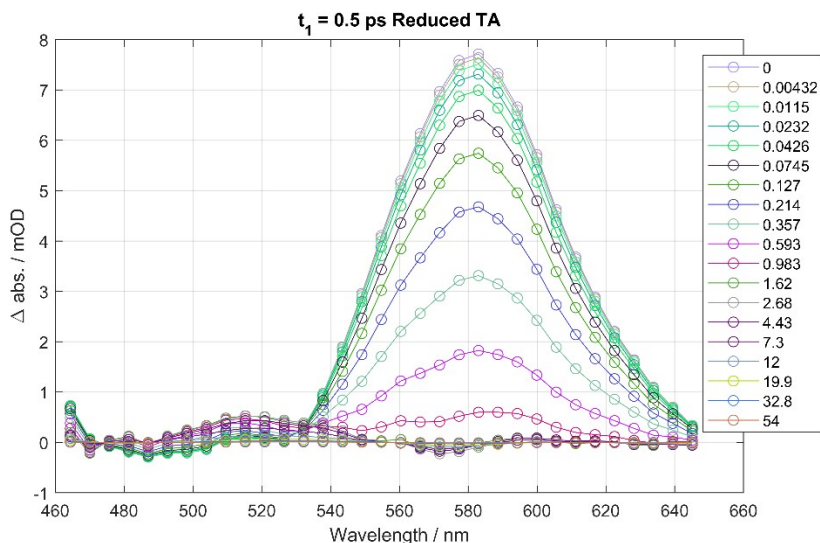

Figure S7. Reduced TA spectra for the 3-pulse data with t_1 = 0.5 ps. The t_2 delays in ps are shown as inset.

A new global fit was performed for reduced TA spectra using exponential decay function using one component and two components. The spectral shapes of the obtained DAS for two-component fit (Fig. S8a) represent mirror images of each other, and the obtained characteristic times are same as well. These observations convey that one component fit is sufficient. The DAS component fit (Fig. S8b) shows the same shape and characteristic time as before.
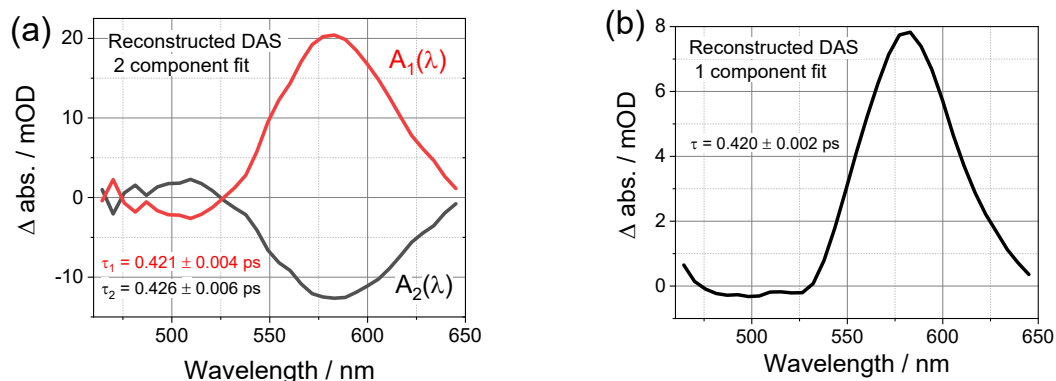

Figure S8. Reconstructed DAS for t_1 = 0.5 ps using two-component fit (a) and one-component fit (b).

S9. Additional experimental results for long t_1 delay scans (t_1=10 ps, and 200 ps)

The raw spectra and DAS for all long t_1 delay scans ($t_1 \geq 10$ ps) have been shown (Fig. S9 a-c, and D-F respectively) along with the results for already demonstrated t_1=50 ps scans in the main text. It can be observed that the spectral shapes of raw spectra and DAS, and the characteristic times are almost similar for each t_1 scan. Therefore, the involved species and their behavior are almost same at long t_1 delays thus considering one long t_1 scan experiment is sufficient to characterize the corresponding processes and species.
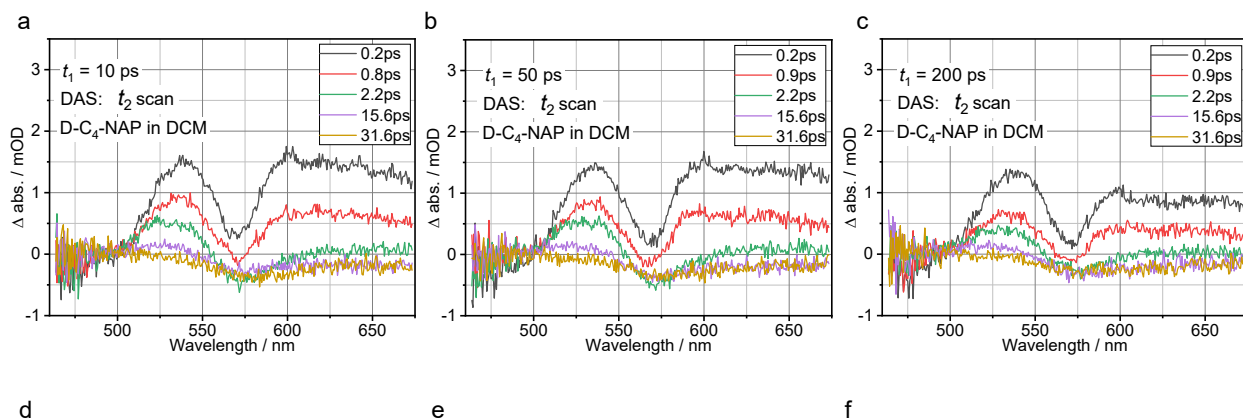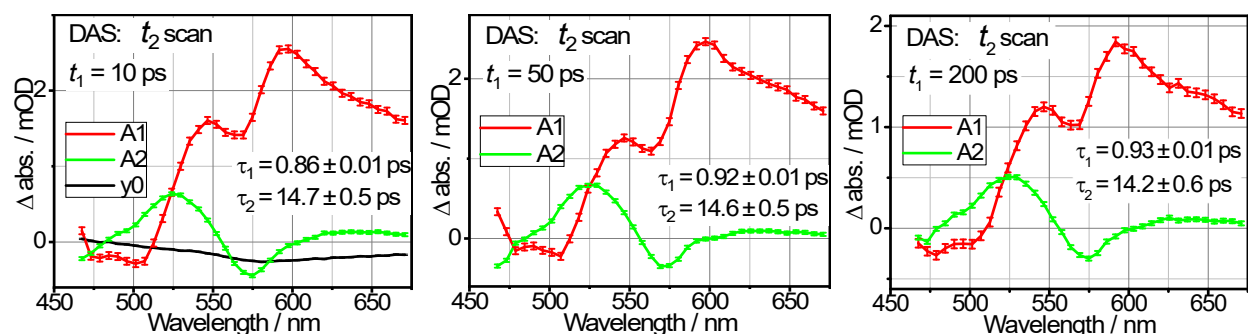
Figure S9. 3-Pulse t_2-scan raw spectra (a-c), and DAS spectra (d-f) for the data sets with t_1 of 10 ps and 200 ps for D-C4-NAP in DCM respectively. The characteristic times are shown as insets.

S10. Details of TD-DFT calculations and natural transition orbital overlap analysis for $S_1 \rightarrow S_n$ transitions

DFT and TD-DFT calculations were performed employing the MN15 functional and the Def2-SVP basis set as implemented in Gaussian 16, Revision A.03. The MN15 functional was chosen as it gives a closer agreement between the experimental vibrational frequencies and electronic spectra. For the simulation of solvent effects, polarizable continuum model (PCM) was used. Fixed torsion angles between D and A moieties, 0, 15, 30, 60, 75, and 90°, were used when evaluating the torsion angle dependent parameters associated with vibrational spectra. Projected frequencies were determined in cases where torsional conformations do not correspond to energy minima. Natural Transition Orbital analysis was conducted to identify the nature of the electronic transitions.

Natural transition orbitals of $S_1 \rightarrow S_2$ and $S_1 \rightarrow S_3$ transitions are shown in Figure S11. We found that the NTO are similar at different θ angles, supporting the assignment of similar spectra to S1A and S1B. At the same time, we do see some changes in NTO as a function of θ. These changes agree with our previous evaluation of the permanent dipole moment changes with θ: the S1 dipole moment is the smallest for the most planar conformation,[1] which can be seen in Figure S10(left) as the highest protrusion of the receiving orbital towards the donor at small θ angles, compared to that for large θ angles.
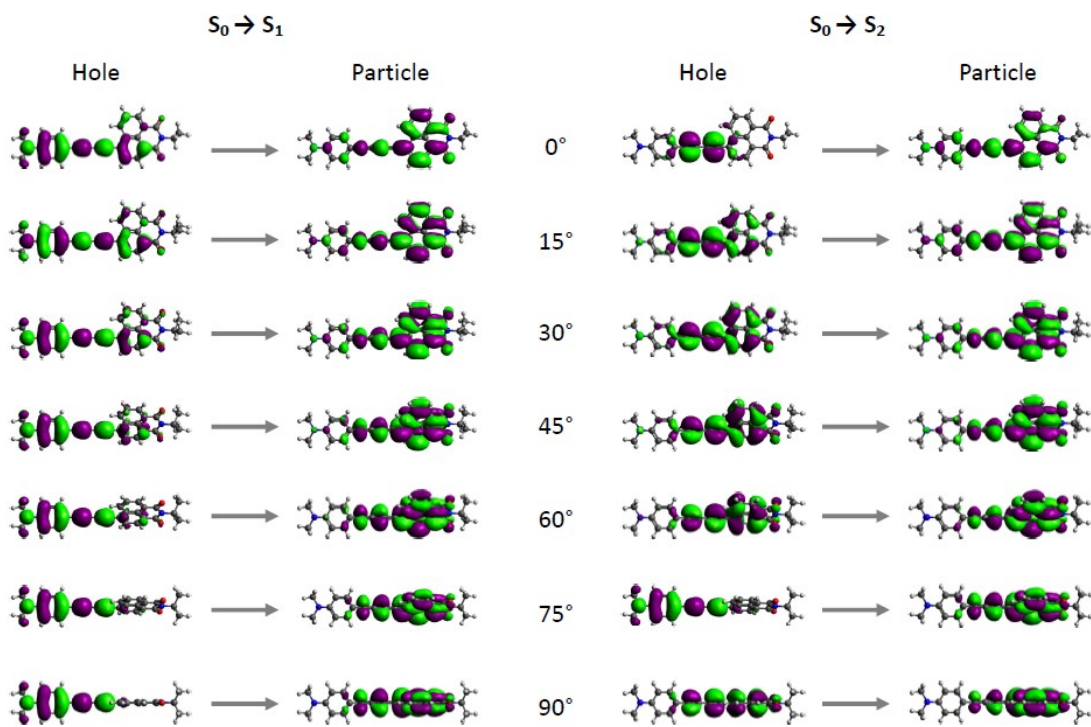
Figure S10. Qualitative NTO analysis for $S_0{\rightarrow}S_1$ and $S_0{\rightarrow}S_2$ transitions.
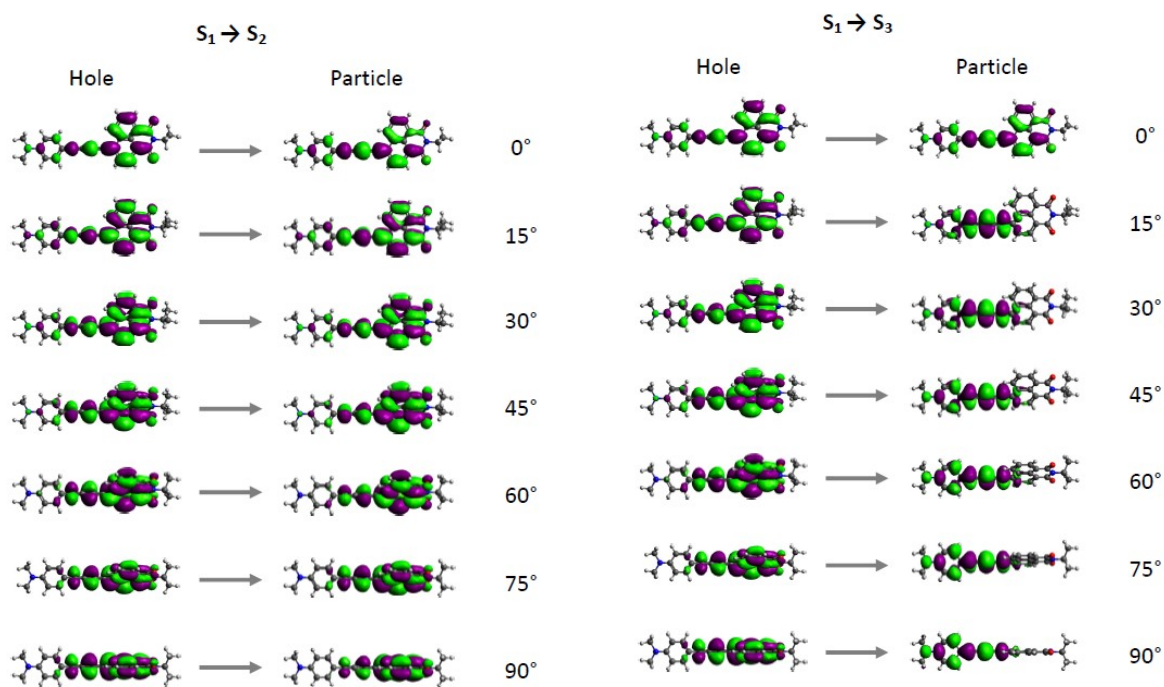

Figure S11. Qualitative NTO analysis for $S_1{\rightarrow}S_n$ transitions.

S11. Butadiyne bridged DBAs

DBA compounds featuring C4 bridge, NAP acceptor and different donors, Si-C4-NAP, Ph-C4-NAP, and D-C4-NAP, are shown in Figure S12.
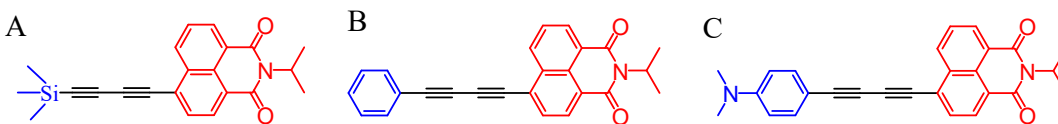

Figure S12. Structures of DBAs featuring butadiyne bridge: (A) Si-C4-NAP, (B) Ph-C4-NAP, and (C) D-C4-NAP.

S12. Evaluation of error bars for k_A^{tr}, k_B^{tr}, and k_B^h

The error bar propagation was performed analytically, where possible, or computationally by deviating the parameters by their error bar values and performing the complete modeling resulting in new values of the final parameters; the deviation of the value of the final parameters were taken as their error bars. As the matrix-based modeling involves many parameters at the same time, each of the parameter was deviated by their error bar; the sign of the deviation of each parameter was taken so that the deviation of the final parameter was additive (not subtractive). The error bars associated with the initial concentrations, involved in the subtraction procedure for k_A^{tr} determination (Eq. S24-26), were taken at 10% of their values. The obtained error bars for the ET rates in vibrationally excited species are shown in Table 2 of the main text.